

Notice: This manuscript submitted to EarthArXiv has not yet been peer reviewed.

1 **Extreme curvature of shallow magma pathways controlled by** 2 **competing stresses**

3 **Timothy Davis¹, Marco Bagnardi^{2,3}, Paul Lundgren³, Eleonora Rivalta^{1,4}**

4 ¹GFZ (GeoForschungsZentrum), Physics of Earthquakes and Volcanoes, Helmholtzstraße 6/7, Building H 7, 14467

5 Potsdam, Germany. {davis,rivalta}@gfz-potsdam.de

6 ²Now at Cryospheric Sciences Laboratory, NASA Goddard Space Flight Center, 8800 Greenbelt Road, Greenbelt, MD,

7 United States. marco.bagnardi@nasa.gov

8 ³Jet Propulsion Laboratory, California Institute of Technology, 4800 Oak Grove Drive, Pasadena, CA, United States.

9 paul.r.lundgren@jpl.nasa.gov

10 ⁴Department of Physics and Astronomy, Alma Mater Studiorum University of Bologna, V.le Berti Pichat 6, Italy.

11 eleonora.rivalta@unibo.it

12 **Summary paragraph**

13 **To feed off-summit eruptions at volcanoes, magma moves by creating and passing through**
14 **cracks that can propagate many kilometres downslope. Typically, these cracks are vertical**
15 **(dykes). Here we analyse the propagation of a flat-lying magma-filled crack (sill) at Sierra**
16 **Negra volcano, Galápagos Islands, using space-borne radar interferometric data spanning**
17 **the 2018 eruption. This sill propagated along a 15-km-long curved trajectory, which is hard**
18 **to explain with current understanding and models. We perform both a simple analytical**
19 **analysis and three dimensional (3D) numerical crack propagation simulations, which in-**
20 **corporate the effects of magma buoyancy, realistic topography and tectonic stresses that**
21 **may control the sill's propagation. We show that sill trajectories can only be understood**
22 **and predicted if accounting for the interaction of all these factors, and explain the observed**
23 **trajectory at Sierra Negra as the result of competing stresses being close to one another through-**

Corresponding author: Timothy Davis, davis@gfz-potsdam.de

24 **out the propagation of the sill. Under certain conditions, these events may be inherently un-**
25 **stable but remain predictable by combining high resolution observations with sophisticated**
26 **theoretical understanding.**

27 **1 Introduction**

28 Sierra Negra is an intra-plate basaltic shield volcano with a maximum elevation of 1140
29 m above sea level (a.s.l.), a shallow (110 m) and structurally complex 7 x 10 km elliptical caldera,
30 and is the most voluminous of the five coalescing volcanoes that form Isabela Island in the west-
31 ern Galápagos Archipelago, Ecuador¹. Thirteen effusive eruptions have occurred at Sierra Ne-
32 gra since 1813. The three most recent eruptions² all occurred in the northern flank of the volcano
33 and produced 0.90 km³ in 1979, 0.15 km³ in 2005, and 0.19 km³ in 2018 . While the 1979 and
34 2005 eruptions were fed by vents high on the northern flank and with eruptive fissures aligned
35 parallel to the caldera rim, the vents of the 2018 eruption were scattered with no preferred ori-
36 entation up to 9.5 km from the caldera rim, at a minimum elevation of 90 m a.s.l. Vents at such
37 low elevation do not seem to be common in the recent history of the volcano. On the other hand,
38 some of the higher-elevation eruptive vents of the 2018 eruption reactivated existing fissures. The
39 2018 eruption interrupted a thirteen-year semi-continuous period of uplift that raised the floor
40 of the summit caldera by up to 5.2 m since the 2005 eruption as measured by GPS (Extended Data
41 Fig. 1), presumed to be re-pressurization of a ~2 km deep magma reservoir. On the 26 June 2018
42 at 19.40 the appearance of volcanic tremor marked the beginning of the eruption. Throughout
43 the eruption, seismicity was mainly located along the caldera fault system with fewer events in
44 the northwestern upper flank. Caldera deflation rapidly started with the onset of eruptive activ-
45 ity and by the time the eruption ended on August 25th 2018, GPS stations measured a cumula-
46 tive intra-caldera subsidence of up to ~8.5 m (Extended Data Fig. 1).

47 Short-lived (< 24 hrs) effusive eruptions from multiple fissures (Fissure 1 - 5, Fig. 1) on
48 26-27 June were followed by a long-lasting effusive eruption from the most distal fissure (Fis-
49 sure 6) between July 1st and August 25th. Geodetic monitoring by continuous GPS at Sierra Ne-

50 gra is limited to the summit caldera, such that the feeder-induced surface displacements were only
51 measured by interferometric synthetic aperture radar (InSAR). The first co-eruptive synthetic aper-
52 ture radar (SAR) image was acquired on 29 June at 17:50 UTC by the Japan Aerospace Explo-
53 ration Agency’s ALOS-2 satellite, approximately 70 hours after the onset of the seismic swarm
54 (Fig. 1). Further SAR images were acquired on 30 June and 1 July by the European Space Agency’s
55 Sentinel-1 satellite constellation, right before the opening of Fissure 6 (Extended Data Fig. 2a
56 and b). Additional SAR images were captured during the eruption of Fissure 6 (Extended Data
57 Fig. 3a and b).

58 Surface deformation patterns before and after Fissure 6 erupted show a surprising trajec-
59 tory for the propagating feeder. The deformation patterns point at a flat-lying magma body (sill,
60 see Methods) with a propagation direction that turned by over 90 degrees, whilst the sill remained
61 flat-lying. Even though turning and twisting of dykes has been observed frequently³⁻⁵, such a 90
62 degree turn has never been observed before.

63 **2 Parameters and numerical result**

64 In order to understand why the sill turned as observed, before proceeding with a 3D sim-
65 ulation, we reduce the physics of this problem to its component parts and evaluate how these af-
66 fect the sill’s direction of propagation. Previous studies have found that dyke trajectories are de-
67 pendent on the ratio of tectonic to topographic loading stresses^{3,6,7}. Here we propose that con-
68 trasting magma and rock weight gradients (buoyancy) must also be considered as one of the dom-
69 inant forces.

70 Propagation directions of dykes have typically been predicted by maximizing the strain en-
71 ergy release rate^{3,8}, on test elongations at the leading tip, thereby finding the path of least resis-
72 tance. Such a method is unwieldy for true 3D propagation, as it would involve computing a large
73 number of potential tip-line growth patterns. Here we use a theoretically equivalent, but more
74 flexible, approach based on the maximum stress intensity, K (see Methods). In our analytical ap-
75 proach, we reduce the sill geometry to that of a penny-shaped crack subject to stress gradients

76 (Supplementary Information), with an opening that is compatible with the surface displacements
 77 observed along the short-axis of the sill (see Methods). At selected points along the sill's path,
 78 we calculate K around the tip-line⁹, and assume the greatest tip-line advance occurs in the direc-
 79 tion where K is largest (Paris fatigue law¹⁰). In our numerical simulations, we discretise the sill
 80 into triangular elements^{10,11} and update the tip-line at each step using the local value of K as com-
 81 pared to the critical rock strength, K_c .

82 In our analytical approach, we employ stress intensity equations in a full-space. We then
 83 go on to numerically test how the free surface and the real topography would affect these results.
 84 In the numerical simulations, we compute stresses under an arbitrary topography in 3D with an
 85 external elastic stress field. As in previous 3D studies we neglect viscous effects of the contained
 86 fluid and chamber pressure.

87 We constrain the parameters in both models using inversions of co-eruptive InSAR data
 88 along the propagation path (Fig. 1, see Methods): depth $d=950$ m, radius $c=1900$ m and volume
 89 $V=1.6\pi c^2$ m³. V represents the volume of the inflated nose of the propagating fracture, which
 90 is around a 10th of the estimated erupted volume² (0.018 km³). We set the rock properties to:
 91 $\rho_r=2900$ kg·m⁻³, $\mu=2\cdot 10^9$ Pa and $\nu=0.35$ corresponding to the rock density, shear modulus
 92 and Poisson's ratio, respectively.

93 **3 Effects defining the sill's path**

94 Opening stress intensity K_I around the edge of a penny-shaped crack of volume V in a full-
 95 space, subject to a constant pressure¹² is:

$$K_I = \frac{3\mu V}{4(1-\nu)c^2\sqrt{\pi c}} \quad (1)$$

96 K_I around a crack under a pressure gradient¹² is:

$$K_{I\alpha} = \frac{4}{3\pi}\Delta\gamma c\sqrt{\pi c}\cos(\alpha) \quad (2)$$

97 where α is the angle away from the direction of the linear stress gradient ($\Delta\gamma$) on the crack's walls.
 98 The pressure gradient in equation (2) defines the direction of K_{max} (blue lines in Fig. 2a). As
 99 such, ignoring other effects, the direction and magnitudes of competing pressure gradients act-
 100 ing on the crack define its propagation direction.

101 We now estimate stress gradients at Sierra Negra. First, we use an analytical solution de-
 102 scribing stresses beneath a ridge-like topography¹³. h and v are the horizontal and vertical axis,
 103 respectively. We compute the horizontal gradient of vertical stress: $\delta\sigma_v/\delta h$, i.e., the normal stress
 104 gradient driving a flat-lying crack away from the caldera rim, at the inferred sill depth along its
 105 track. Linear stress gradients due to the difference between rock and fluid density (buoyancy)¹⁴
 106 are $(\rho_r - \rho_f)g \sin(\beta)$, where ρ_f is the magma density. The factor $\sin(\beta)$ means that if the crack
 107 is flat this gradient is zero. We set¹⁵ $\rho_f = \rho_r - 300 \text{ kg}\cdot\text{m}^{-3}$. For the parameters above, 15 km
 108 from the caldera center (around where the sill began to turn) the dip needs to be around 10° for
 109 the buoyancy gradient to exceed the stress gradient due to the overlying slope (Extended Data
 110 Fig. 4) and drive the sill to turn away from the downslope direction (Fig. 2a).

111 As shown in Extended Data Fig. 5, a dipping sill is attracted towards the free surface. For
 112 $c/d=2$, as observed, a dip of 15° results in the same K_I increase for both buoyancy and free sur-
 113 face, doubling dip's effects.

114 Lastly, we test if the other intrusions to the east that fed fissures 2, 3 and 4 (Fig. 1) may have
 115 attracted the sill. Two penny-shaped cracks subject to equal internal pressure^{12,16} separated 5 km
 116 from each other, as observed (tip separation of 1.2 km) experience a maximal K_I increase of \sim
 117 3%. Such an increase is minor compared to the processes described earlier.

118 To summarise the analytical analysis, the stress gradient due to topography drives the sill
 119 away from the caldera rim. As the slope shallows, the buoyancy gradient begins to dominate even
 120 for shallowly dipping cracks, causing the sill to turn. The free surface amplifies this effect (Ex-
 121 tended Data Fig. 7). This analytical method of assessing the sill path is flexible and fast. In spite
 122 of its simplicity it can explain the trajectory of previous intrusions, including curved dyke trajec-
 123 tories such as the 2014 Bárðarbunga dyke path (Supplementary Information).

124 In order to allow interaction between all factors discussed above, we develop a 3D Bound-
 125 ary Element Model^{9,10} to simulate a penny-shaped crack beneath the real edifice's topography.
 126 We include stresses due to gravitational loading and traction-free boundary conditions on the sur-
 127 face^{9,17}. Using orientations of the crack in the 3D space obtained by inverting surface deforma-
 128 tion (see Methods), our model explains the turning of the sill for snapshots along its path (Fig. 2),
 129 showing that it is the interaction between sill dip, slope gradients and the free surface that causes
 130 the observed turning. Note that increasing the ratio of the horizontal to vertical stress (σ_h/σ_v)
 131 in the topographic loading model results in better fits.

132 **4 Full 3D propagation model**

133 Lastly, we run full 3D fracture propagation simulations¹⁰. Here the crack is neither con-
 134 strained to be planar nor circular in shape, only such that it maintains a constant V . The tip-line
 135 shape is recalculated at every iteration moving it forward in proportion to K/K_c , if $K/K_c >$
 136 1, at each triangle. We remove triangular elements that shut closed. Bending or twisting of the
 137 fracture's tip-line out of its plane is calculated using the maximum circumferential stress crite-
 138 rion¹⁸.

139 In this last approach, we use a planar free surface with a start height at $y = 0$ of 990 m
 140 with a slope of 3° facing to the north. The lithostatically stressed body ($\sigma_h = \sigma_v$) is loaded
 141 due to topography¹³ (Extended Data Fig. 4). We also apply throughout the body a compressive
 142 tectonic stress of 4.5 MPa directed along σ_{yy} , with σ_{xx} the mean between σ_{yy} and σ_{zz} , as sug-
 143 gested by stress indicators¹⁹. Shear stresses from the topographic loading solution¹³ are set to
 144 zero, on the assumption that these stresses are diminished over time by faulting, diking and longer
 145 term rock deformation processes in the edifice's flanks.

146 The initial crack is an ellipse 1000 m wide and 5000 m long at a depth of 1000 m below
 147 sea level, dipping to the west by $\beta=1^\circ$. K_c is set to $70 \text{ MPa}\cdot\text{m}^{0.5}$. We find when the fracture gets
 148 a certain distance away from the caldera centre, it begins to turn and propagates east (Fig. 3). By
 149 changing the values of the parameters one at a time, we investigate the sensitivity of the path to

150 the input parameters and initial geometry (Fig. 4). Reducing the initial start dip β or the buoy-
151 ancy reduces the force driving the sill eastwards, causing the sill to stall as the topography shall-
152 lows (Fig. 4, curves B to E). The start depth defines when the free surface attraction takes effect
153 (Extended Data Fig. 7F), such that only shallower sills can propagate eastwards (Fig. 4, curves
154 F,G). The fracture toughness and volume define how far the sill can travel downslope as the to-
155 pography shallows. These also control the sill width, reducing the buoyancy force when this is
156 smaller, again trapping the sill (Fig. 4, curves H to K). When the tectonic compressive stress is
157 reduced, in places σ_v becomes the most compressive stress, causing the sills track to become very
158 unstable with the sill quickly rising to the surface (Fig. 4L).

159 The simulations compare well with the observed trajectory; the sill was destined to turn,
160 although it could have stalled or erupted earlier on its path.

161 5 Conclusions

162 Previous flank volcanism at Galápagos volcanoes has been fed by radial and circumferen-
163 tial dykes^{4,20}. Here we have shown evidence of flank volcanism fed by a long curving sill. We
164 find that trajectories of shallow sills underneath topography will be unstable and defined by a del-
165 icate balance between buoyancy forces, topographic load, external stresses and the free surface.
166 Still, trajectories may be anticipated, provided all those factors are well-constrained and their in-
167 teraction is accounted for. By combining such models with careful analysis of high-resolution
168 crustal deformation data, we showed that such parameters as well as the state of stress of the vol-
169 cano can be well constrained, reducing the uncertainties in the hazard.

170 Main references

- 171 1. Reynolds, R. W., Geist, D. & Kurz, M. D. Physical volcanology and structural develop-
172 ment of Sierra Negra volcano, Isabela island, Galápagos archipelago. *Geological Society
173 of America Bulletin* **107**, 1398–1410 (1995).

- 174 2. Vasconez, F. J. *et al.* The different characteristics of the recent eruptions of Fernandina and
175 Sierra Negra volcanoes (Galápagos, Ecuador). *Volcanica* **1**, 127–133 (2018).
- 176 3. Sigmundsson, F. *et al.* Segmented lateral dyke growth in a rifting event at Bárðarbunga
177 volcanic system, Iceland. *Nature* **517**, 191–195 (2015).
- 178 4. Bagnardi, M., Amelung, F. & Poland, M. P. A new model for the growth of basaltic shields
179 based on deformation of Fernandina volcano, Galápagos Islands. *Earth and Planetary Sci-*
180 *ence Letters* **377**, 358–366 (2013).
- 181 5. Smittarello, D. *et al.* Magma propagation at Piton de la Fournaise from joint inversion of
182 InSAR and GNSS. *Journal of Geophysical Research: Solid Earth* **124**, 1361–1387 (2019).
- 183 6. Roman, A. & Jaupart, C. The impact of a volcanic edifice on intrusive and eruptive activ-
184 ity. *Earth and Planetary Science Letters* **408**, 1–8 (2014).
- 185 7. Rivalta, E. *et al.* Stress inversions to forecast magma pathways and eruptive vent location.
186 *Science advances* **5**, eaau9784 (2019).
- 187 8. Dahm, T. Numerical simulations of the propagation path and the arrest of fluid-filled frac-
188 tures in the Earth. *Geophysical Journal International* **141**, 623–638 (2000).
- 189 9. Davis, T., Healy, D. & Rivalta, E. Slip on wavy frictional faults: Is the 3rd dimension a
190 sticking point? *Journal of Structural Geology* **119**, 33–49 (2019).
- 191 10. Davis, T., Rivalta, E. & Dahm, T. Critical fluid injection volumes for uncontrolled frac-
192 ture ascent. *Geophysical Research Letters*, e2020GL087774 (2020).
- 193 11. Nikkhoo, M. & Walter, T. R. Triangular dislocation: an analytical, artefact-free solution.
194 *Geophysical Journal International* **201**, 1119–1141 (2015).
- 195 12. Tada, H., Paris, P. & Irwin, G. *The Stress Analysis of Cracks Handbook; Third edition* 1
196 (New York: ASME Press, 2000).
- 197 13. Savage, W. Z., Powers, P. S. & Swolfs, H. S. *In situ geomechanics of crystalline and sed-*
198 *imentary rocks; Part V, RVT, a Fortran program for an exact elastic solution for tecton-*
199 *ics and gravity stresses in isolated symmetric ridges and valleys* tech. rep. (US Geolog-
200 ical Survey, Denver, Colorado, 1984).

- 201 14. Pollard, D. D. & Townsend, M. R. Fluid-filled fractures in Earth's lithosphere: Gravitational loading, interpenetration, and stable height of dikes and veins. *Journal of Structural*
202 *Geology* **109**, 38–54 (2018).
- 204 15. Vigouroux, N. *et al.* 4D gravity changes associated with the 2005 eruption of Sierra Negra volcano, Galápagos. *Geophysics* **73**, WA29–WA35 (2008).
- 206 16. Fabrikant, V. Close interaction of coplanar circular cracks in an elastic medium. *Acta Mechanica* **67**, 39–59 (1987).
- 208 17. Martel, S. J. Modeling elastic stresses in long ridges with the displacement discontinuity method. *Pure and Applied Geophysics* **157**, 1039–1057 (2000).
- 210 18. Pollard, D., Pollard, D. D., Fletcher, R. C. & Fletcher, R. C. *Fundamentals of structural geology* (Cambridge University Press, 2005).
- 212 19. Heidbach, O. *et al.* The World Stress Map database release 2016: Crustal stress pattern across scales. *Tectonophysics* **744**, 484–498 (2018).
- 214 20. Chadwick Jr, W. & Dieterich, J. Mechanical modeling of circumferential and radial dike intrusion on Galapagos volcanoes. *Journal of Volcanology and Geothermal Research* **66**,
215 37–52 (1995).
- 217 21. Rosen, P., Gurrola, E., Agram, P. S., Sacco, G. F. & Lavalle, M. The InSAR Scientific Computing Environment (ISCE): A python framework for Earth science. *AGUFM* **2015**, IN11C–
218 1789 (2015).
- 220 22. Wessel, B. *et al.* Accuracy assessment of the global TanDEM-X Digital Elevation Model with GPS data. *ISPRS Journal of Photogrammetry and Remote Sensing* **139**, 171–182 (2018).
- 222 23. Chen, C. W. & Zebker, H. A. Two-dimensional phase unwrapping with use of statistical models for cost functions in nonlinear optimization. *JOSA A* **18**, 338–351 (2001).
- 224 24. Bagnardi, M. & Hooper, A. Inversion of surface deformation data for rapid estimates of source parameters and uncertainties: A Bayesian approach. *Geochemistry, Geophysics, Geosystems* **19**, 2194–2211 (2018).
- 226

- 227 25. Decriem, J. *et al.* The 2008 May 29 earthquake doublet in SW Iceland. *Geophysical Jour-*
228 *nal International* **181**, 1128–1146 (2010).
- 229 26. Okada, Y. Surface deformation due to shear and tensile faults in a half-space. *Bulletin of*
230 *the seismological society of America* **75**, 1135–1154 (1985).
- 231 27. Sun, R. J. Theoretical size of hydraulically induced horizontal fractures and correspond-
232 ing surface uplift in an idealized medium. *Journal of Geophysical Research* **74**, 5995–6011
233 (1969).

Fig. 1. Interferogram spanning the sill propagation phase of the 2018 eruption. SAR data from the ALOS-2 satellite. Each colour cycle represents 11.45 cm of line-of-sight (LOS) surface displacement. Gray polygons show the extent of the lava flows emplaced during the time period spanned by the interferogram. Yellow lines mark the location and extent of all eruptive fissures. Black triangles mark the location of GPS stations. Black arrows show the satellite orbit direction (\sim N-S), look direction (\sim E-W), and the incidence angle in degrees. Descending pass, Track 147, ScanSAR mode.

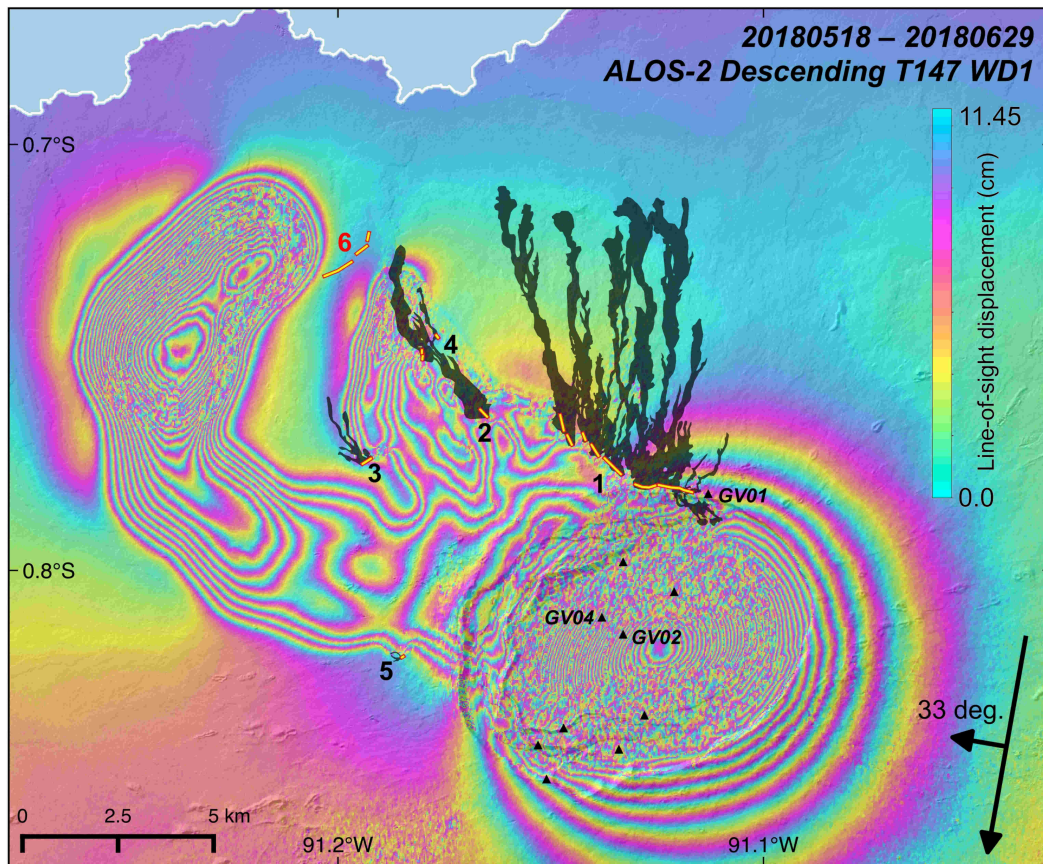


Fig. 2. Simulating the propagation direction of fracture at selected locations a) Analytical K_I diagram.

Black circles represent the fracture, distance of the dashed gray line to the fracture edge represents K_I magnitude, blue segment represents K_{max} direction. Topographic contours in orange. b) Numerical simulation of the propagation direction at Sierra Negra. Fractures are scaled down to a 1 km radius, white dashed-line represents K_I magnitude as in a). Dip and strike directions shown, defined by inversions (see Methods). For P7 a dip of 15° is used. Dashed grey outline is a contour of sill-induced deformation from Extended Data

Fig. 3. Background $\sigma_h/\sigma_v=0.5$ in topographic loading model.

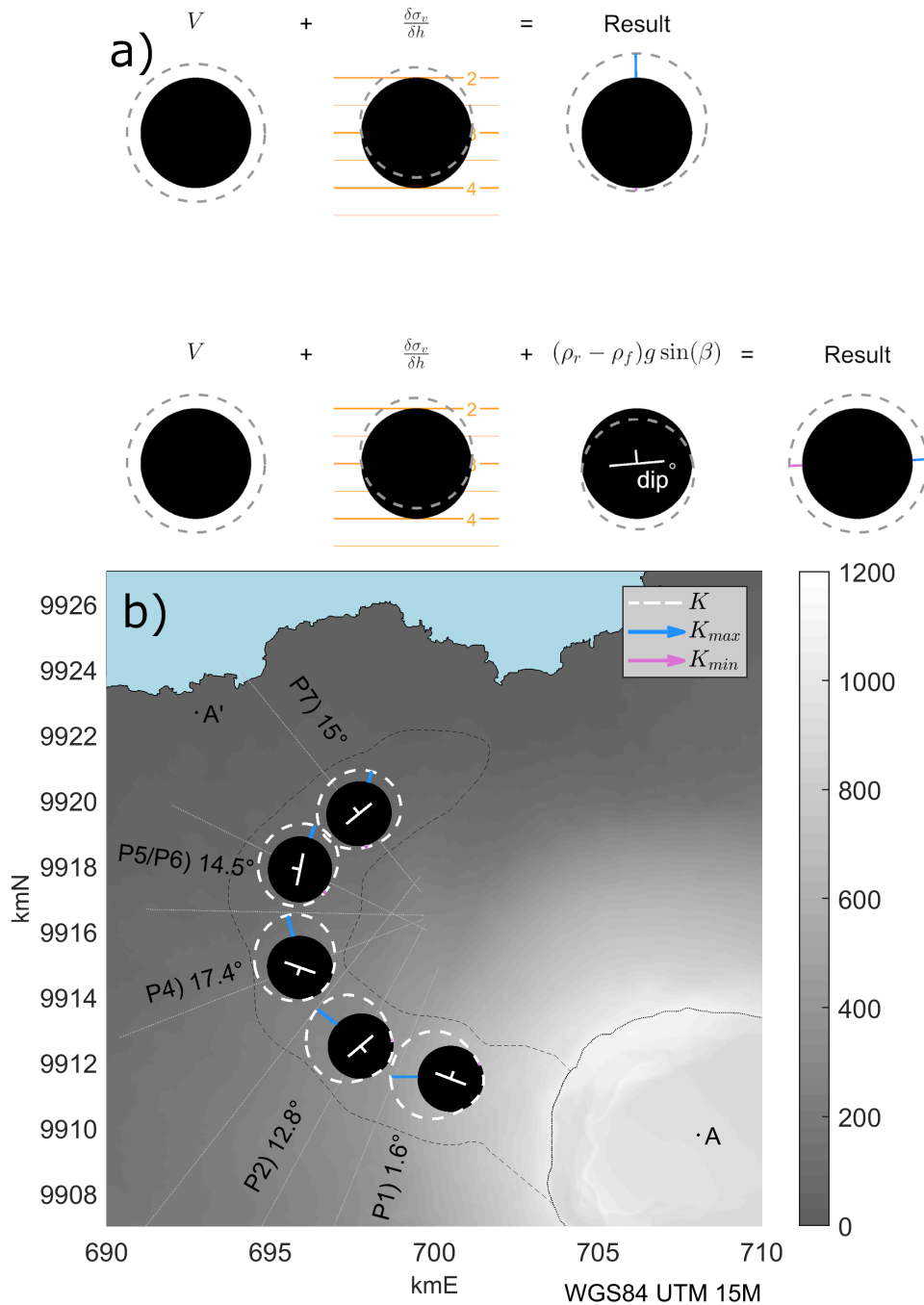


Fig. 3. Numerical simulation of the sill propagation. a) Map view, b) cross-section looking along the downslope direction and c) cross-section looking along the x -axis c). The fracture is shown at chosen locations along its computed path. Grey points are edges that closed in the previous iteration. The shaded patch in a) is the sill track and the dotted line is the caldera rim. In c) the solid line is the topographic slope used to load the body and the dashed line is the simulations free surface. Parameters used: $\beta = 1^\circ$, $\rho_f = \rho_r - 300$ kg/m³, start depth of 1000 m, $K_c = 70$ MPa \cdot m^{0.5}, $V = 1.6\pi c^2$ m³ and $\sigma_{yy} = -4.5$ MPa.

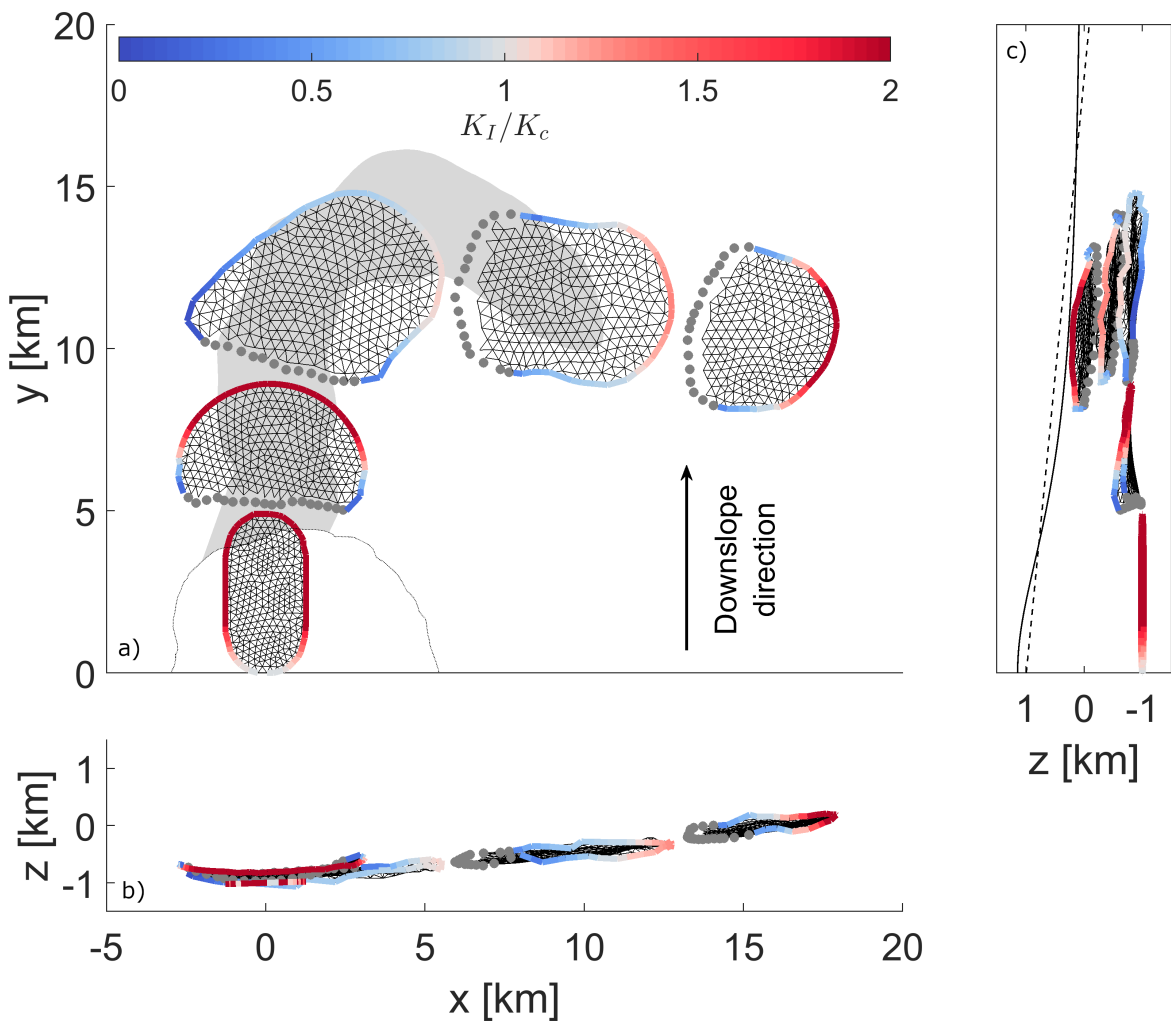
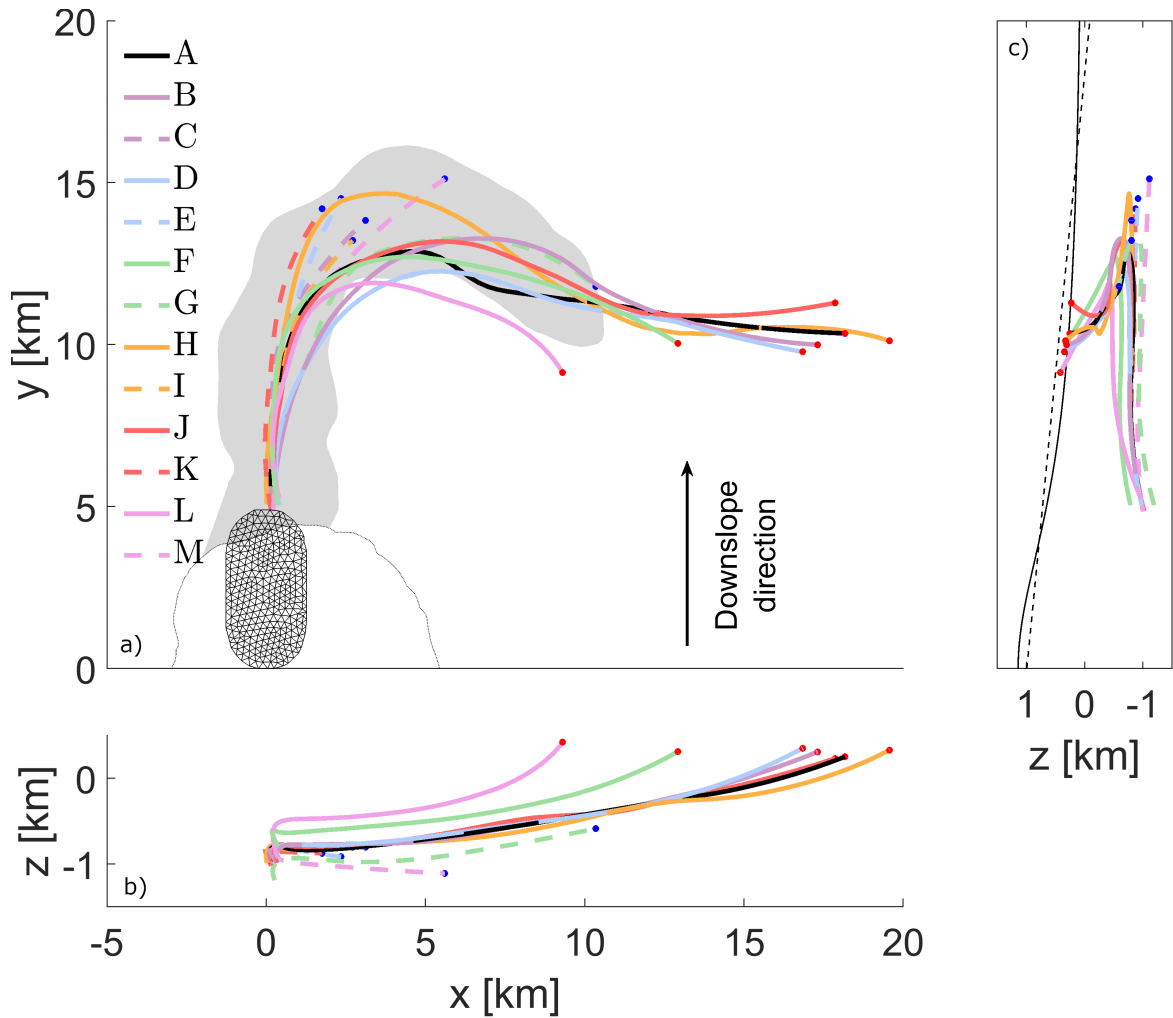


Fig. 4. Effects of parameters on the simulated sill path. Fracture paths from simulations as in Fig. 3, defined by the triangle with the maximum K value at each iteration. Dashed lines with blue dots are fractures that stalled, solid lines with red dots reached the free surface (erupted). In each simulation we changed one parameter with respect to Fig. 3, as follows: A is reference simulation from Fig. 3, B: $\beta = 1.5^\circ$, C: $\beta = 0.5^\circ$, D: $\rho_f = \rho_r - 450 \text{ kg/m}^3$, E: $\rho_f = \rho_r - 150 \text{ kg/m}^3$, F: Start depth=800 m, G: Start depth=1200 m, H: $K_c = 55 \text{ MPa} \cdot \text{m}^{0.5}$, I: $K_c = 85 \text{ MPa} \cdot \text{m}^{0.5}$, J: $V = 1.8\pi c^2 \text{ m}^3$, K: $V = 1.4\pi c^2 \text{ m}^3$, L: $\sigma_{yy} = -3 \text{ MPa}$, M: $\sigma_{yy} = -6 \text{ MPa}$.



234 **Methods**

235 **GPS data**

236 Extended Data Fig. 1 shows the continuous GPS time series for three stations located at
 237 the summit of Sierra Negra (see Fig. 1 for station locations). Data downloaded from [http://](http://geodesy.unr.edu)
 238 geodesy.unr.edu.

239 **Definition of K**

240 The total stress intensity which is compared to the fracture toughness at a point of a cracks
 241 tip-line can be defined by a combination of the opening, sliding and tearing mode stress inten-
 242 sity factors¹⁸ (K_I , K_{II} and K_{III}).

$$K = \sqrt{K_I^2 + K_{II}^2 + \left(\frac{1}{1-\nu}\right) K_{III}^2} \quad (3)$$

243 which relates to strain energy release rate¹² (\mathcal{G}) through:

$$K = \sqrt{\frac{\mathcal{G}E}{1-\nu^2}}; \quad (4)$$

244 where E is the Young's modulus.

245 **InSAR processing and additional observations**

246 All interferograms were created using the InSAR Scientific Computing Environment (ISCE)
 247 software²¹ and by applying conventional differential InSAR processing techniques for stripmap,
 248 ScanSAR (ALOS-2), and Terrain Observation by Progressive Scans (TOPS) (Sentinel-1) data.
 249 Topographic contributions to the interferometric phase are removed using the Deutsches Zentrum
 250 für Luft und Raumfahrt (DLR) 12-m resolution digital elevation model based on TanDEM-X satel-
 251 lite measurements²², and interferograms are phase-unwrapped using the Statistical-cost, Network-
 252 flow Algorithm for Phase Unwrapping (SNAPHU)²³ implemented in ISCE.

253 **InSAR inversions along track**

254 Deformation source parameters and uncertainties are estimated using a Bayesian approach
255 implemented in the Geodetic Bayesian Inversion Software²⁴. The inversion algorithm samples
256 posterior probability density functions (PDFs) of source parameters using a Markov chain Monte
257 Carlo method, incorporating the Metropolis-Hastings algorithm, with automatic step size selec-
258 tion. Posterior PDFs are calculated considering errors in the InSAR data, which we directly quan-
259 tify using experimental semivariograms to which we fit an unbounded exponential one-dimensional
260 function with a nugget²⁴. The exponential function is then used to populate the data variance-covariance
261 matrix. Prior to inversions, all InSAR data sets are subsampled using an adaptive quadtree sam-
262 pling²⁵ to reduce the computational burden when calculating the inverse of the data variance-covariance
263 matrix and in forward model calculations. For all models, we assume that the deformation sources
264 are embedded in an isotropic elastic half-space with Poisson's ratio $\nu = 0.25$. Since no detailed
265 prior information on the deformation source parameters are available, prior probability distribu-
266 tions are assumed to be uniform between geologically realistic bounds. In each inversion, pos-
267 terior PDFs are sampled through 10^6 iterations. Depth estimates are referred to as distance from
268 the surface.

269 At profile locations P1, P4 and P5 in Extended Data Fig. 6 we estimate source parameters
270 of a rectangular dislocation with constant opening²⁶ and retrieve openings of 0.74 ± 0.03 , 1.73 ± 0.03
271 and 2.80 ± 0.03 m respectively, where the value after \pm brackets the 2.5 and 97.5 percentile of
272 the results from our Bayesian inversion scheme²⁴ (Extended Data Table. 1). Using such solutions
273 the depth of this sill along its path is consistently 900-1000 m below the ground surface with a
274 half-width of approximately 1.5 km.

275 **Choosing physical parameters**

276 We approximate the sill in our analytical analysis as a penny shaped crack. To retrieve c
277 and V for this geometry, we compare the ground deformation of a flat lying rectangular disloca-
278 tion where the faces open 2 m with a depth d of 950 m and its third axis extending far out of the

279 plane of observation, to the analytical solution describing the uplift due to a pressurised penny-
 280 shaped crack under a half-space²⁷ with the same d . The penny-shaped crack's ground deforma-
 281 tion supplies a radial deformation pattern, therefore we only fit this to the ground deformation
 282 relative to the short-axis of the sill. Once fitted, we retrieve a radius $c=1900$ m and volume $V =$
 283 $1.6\pi c^2$ (with the largest error 1.5% and 15% less than the maximum u_z and u_x value from the
 284 dislocation solution, respectively).

285 **Comparison of different effects on stress intensity factors**

286 Extended Data Fig. 5 is computed using a numerical scheme to evaluate how K_I in equa-
 287 tion (1), decreases as the crack approaches the free surface⁹. For $c/d=2$ as observed, a dip of 15°
 288 causes a relative increase and decrease of K_I of +30% and -10% at its highest and lowest edge
 289 respectively. A 30% increase corresponds to the same K_I increase as a sill dip of around 15° due
 290 to $(\rho_r - \rho_f)g \sin(\beta)$. As with buoyancy, this effect increases with crack dip.

291 **End notes**

292 **Data availability statement**

293 Computed interferograms that support the findings of this study are achieved as geoTIFF
 294 files on Zenodo at <http://...> Sentinel-1 raw SAR data that support the findings of this study are
 295 publicly available at <https://scihub.copernicus.eu>. ALOS-2 raw SAR data availability is restricted
 296 to PI investigation at www.eorc.jaxa.jp/ALOS/en/.

297 **Code availability statement**

298 The code used for boundary element numerical analysis in this study was the open source
 299 code <https://doi.org/10.5281/zenodo.3694163> with an interface with the Com-
 300 putational Geometry Algorithms Library software (C++) for meshing.

301 **Acknowledgements**

302 T Davis is funded by the DFG-ICDP grant N. RI 2782/3-1. M. Bagnardi was supported by
303 an appointment to the NASA Postdoctoral Program at the Jet Propulsion Laboratory, adminis-
304 tered by the Universities Space Research Association (USRA) through a contract with NASA.
305 Part of this research was carried out at the Jet Propulsion Laboratory, California Institute of Tech-
306 nology, under a contract with the National Aeronautics and Space Administration (grant 281945.02.47.04.51).

307 **Author Contributions**

308 T.D and M.B coordinated the work and wrote the initial manuscript. M.B and P.L acquired
309 and analysed the InSAR and GPS data in this study. This analysis provided the evolution and ge-
310 ometry of the sill. T.D and E.R conceptualised the analytical and numerical fracture mechanics
311 that form the interpretation in this work. T.D wrote the analytical and numerical fracture mechan-
312 ics codes used in this study. All authors have read and revised the manuscript and contributed
313 ideas to the research.

314 **Additional Information**

315 Supplementary Information is available for this paper. Correspondence and requests for
316 materials should be addressed to T.Davis.

317 **Methods references**

- 318 9. Davis, T., Healy, D. & Rivalta, E. Slip on wavy frictional faults: Is the 3rd dimension a
319 sticking point? *Journal of Structural Geology* **119**, 33–49 (2019).
- 320 12. Tada, H., Paris, P. & Irwin, G. *The Stress Analysis of Cracks Handbook; Third edition* 1
321 (New York: ASME Press, 2000).
- 322 18. Pollard, D., Pollard, D. D., Fletcher, R. C. & Fletcher, R. C. *Fundamentals of structural*
323 *geology* (Cambridge University Press, 2005).

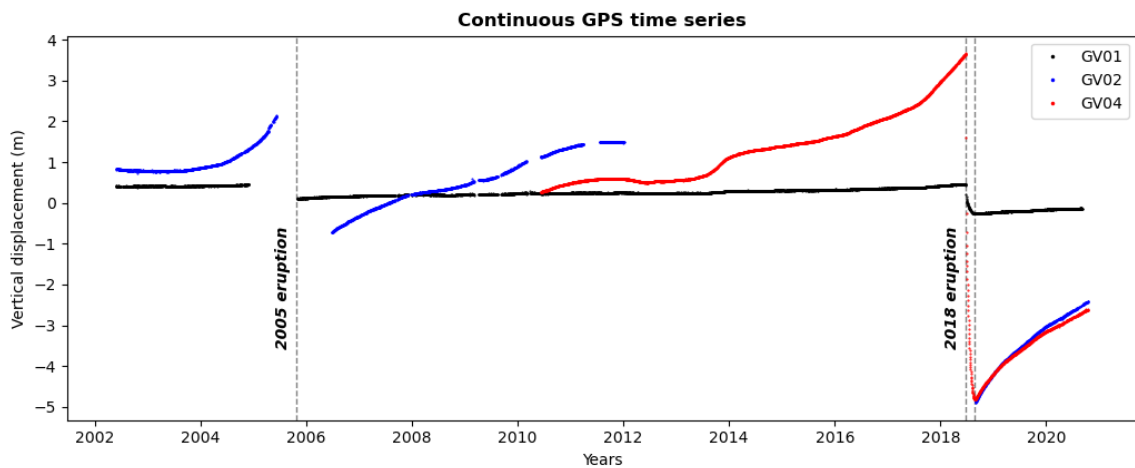
- 324 21. Rosen, P., Gurrola, E., Agram, P. S., Sacco, G. F. & Lavalle, M. The InSAR Scientific Com-
 325 puting Environment (ISCE): A python framework for Earth science. *AGUFM* **2015**, IN11C–
 326 1789 (2015).
- 327 22. Wessel, B. *et al.* Accuracy assessment of the global TanDEM-X Digital Elevation Model
 328 with GPS data. *ISPRS Journal of Photogrammetry and Remote Sensing* **139**, 171–182 (2018).
- 329 23. Chen, C. W. & Zebker, H. A. Two-dimensional phase unwrapping with use of statistical
 330 models for cost functions in nonlinear optimization. *JOSA A* **18**, 338–351 (2001).
- 331 24. Bagnardi, M. & Hooper, A. Inversion of surface deformation data for rapid estimates of
 332 source parameters and uncertainties: A Bayesian approach. *Geochemistry, Geophysics, Geosys-*
 333 *tems* **19**, 2194–2211 (2018).
- 334 25. Decriem, J. *et al.* The 2008 May 29 earthquake doublet in SW Iceland. *Geophysical Jour-*
 335 *nal International* **181**, 1128–1146 (2010).
- 336 26. Okada, Y. Surface deformation due to shear and tensile faults in a half-space. *Bulletin of*
 337 *the seismological society of America* **75**, 1135–1154 (1985).
- 338 27. Sun, R. J. Theoretical size of hydraulically induced horizontal fractures and correspond-
 339 ing surface uplift in an idealized medium. *Journal of Geophysical Research* **74**, 5995–6011
 340 (1969).

341 **Extended Data**

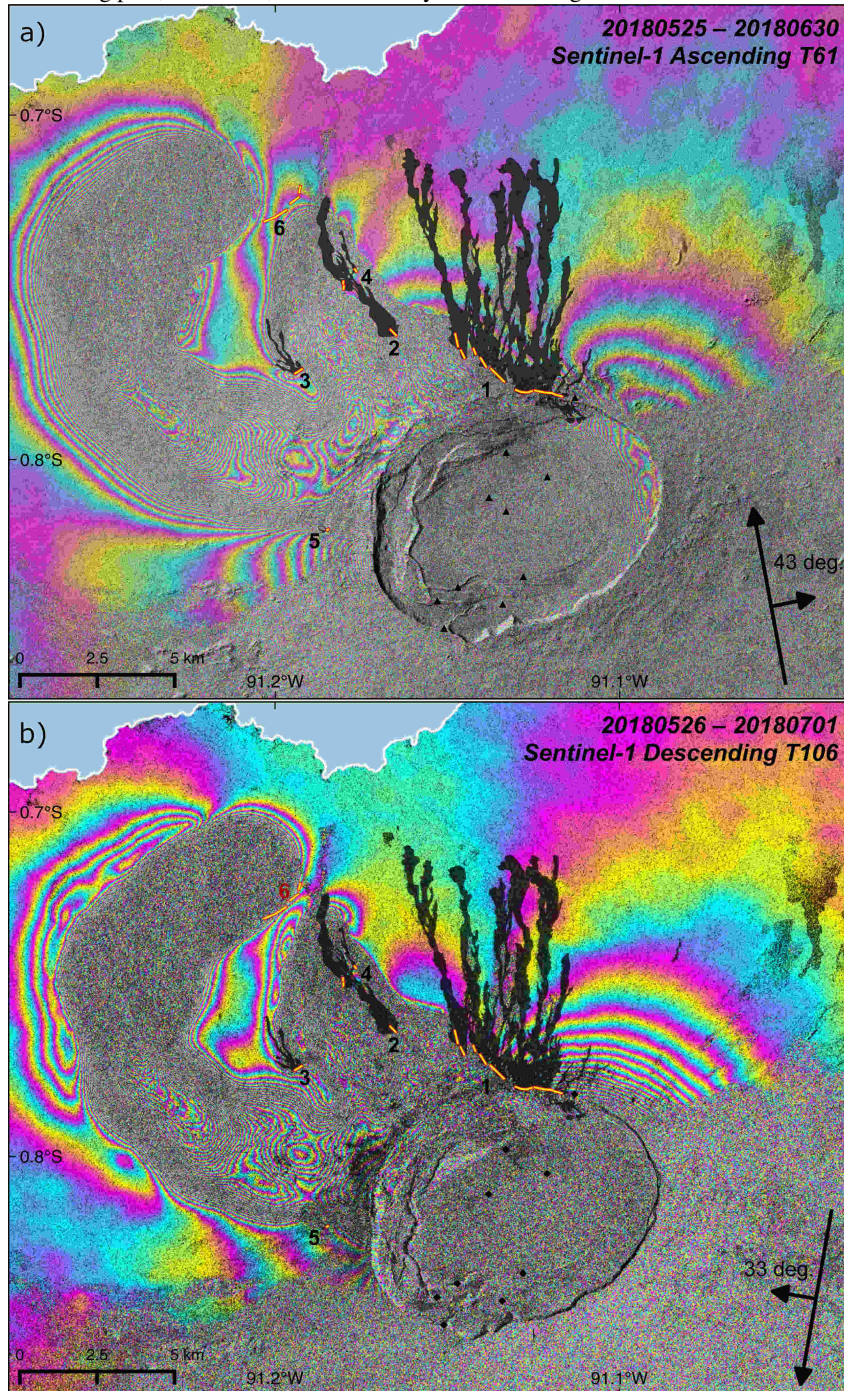
Extended Data Table 1. Bayesian inversion results for profiles shown in Extended Data Fig. 6, using rectangular dislocations²⁶. The 2.5 percentile value, the maximum a posteriori probability solution, and the 97.5 percentile value are shown for each parameter. The results for P7 are not shown, due to unsatisfactory fits to the data.

Profile	Opening [m]	Dip ^o	Dip Direction ^o	Depth [m]	Down-dip width [m]	Along-strike width [m]
P1	0.7 / 0.7 / 0.8	0.6 / 1.6 / 2.7	19 / 21 / 23	861 / 899 / 958	2907 / 2949 / 2986	2554 / 3175 / 4503
P2	1.0 / 1.0 / 1.0	11.0 / 12.8 / 15.4	136 / 140 / 142	998 / 1058 / 1335	2527 / 2637 / 3787	2356 / 2387 / 2421
P3	1.2 / 1.2 / 1.2	3.0 / 5.5 / 7.5	138 / 140 / 142	939 / 992 / 1040	3541 / 3891 / 13903	2119 / 2140 / 2172
P4	1.7 / 1.8 / 1.8	16.7 / 17.4 / 18.1	199 / 199 / 200	1053 / 1084 / 1115	3296 / 3604 / 3653	1754 / 1771 / 1789
P5	2.8 / 2.8 / 2.8	14.0 / 14.5 / 15.0	210 / 210 / 210	994 / 1010 / 1026	2196 / 2210 / 2224	2838 / 2850 / 2859
P6	2.80 / 2.83 / 2.85	14.1 / 14.6 / 14.9	352 / 353 / 353	976 / 993 / 1007	2322 / 2340 / 2353	2826 / 2840 / 2851

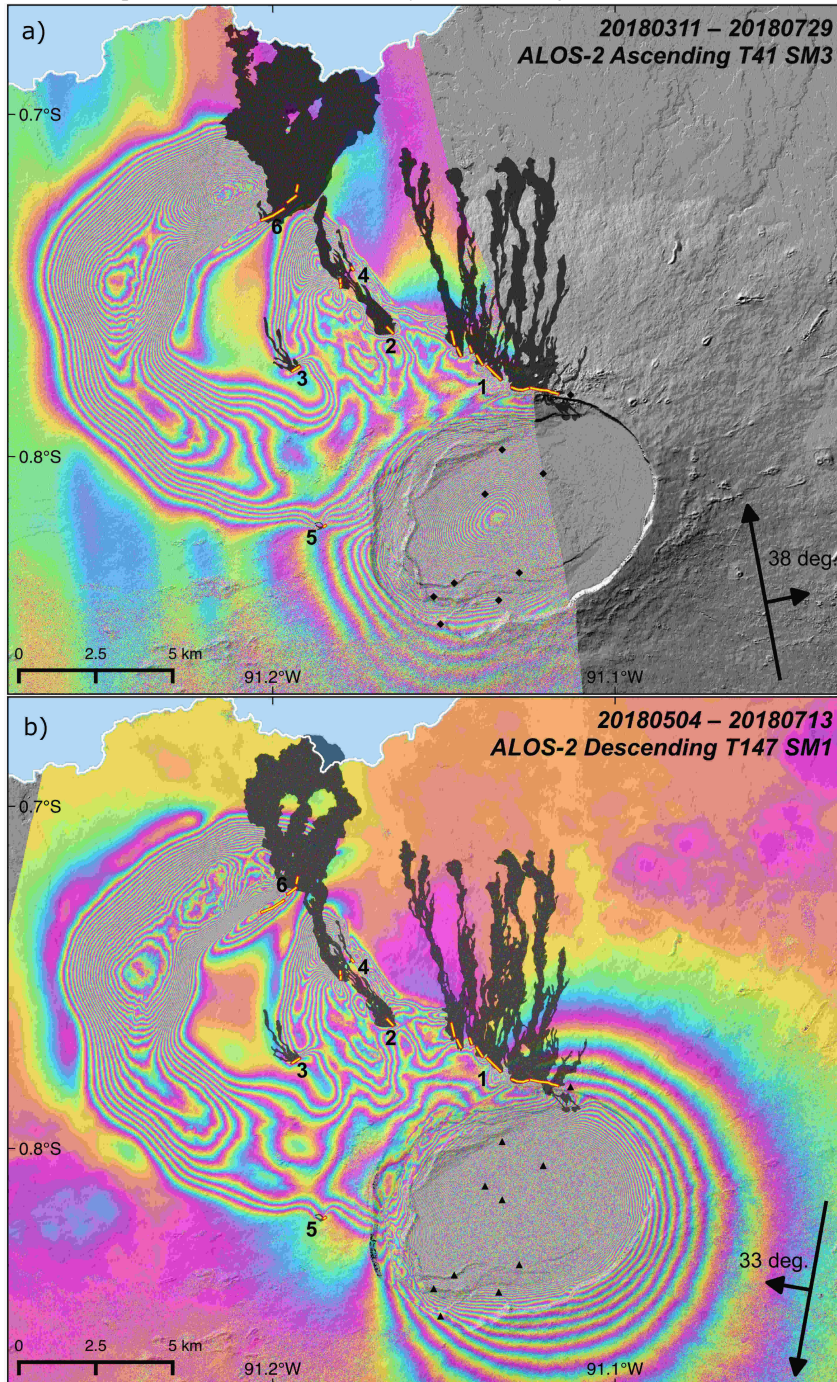
Extended Data Fig. 1. Vertical GPS movement's from continuous GPS stations GV01, 02 and 04 situated on Sierra Negra's summit. See Fig. 1 for station location.



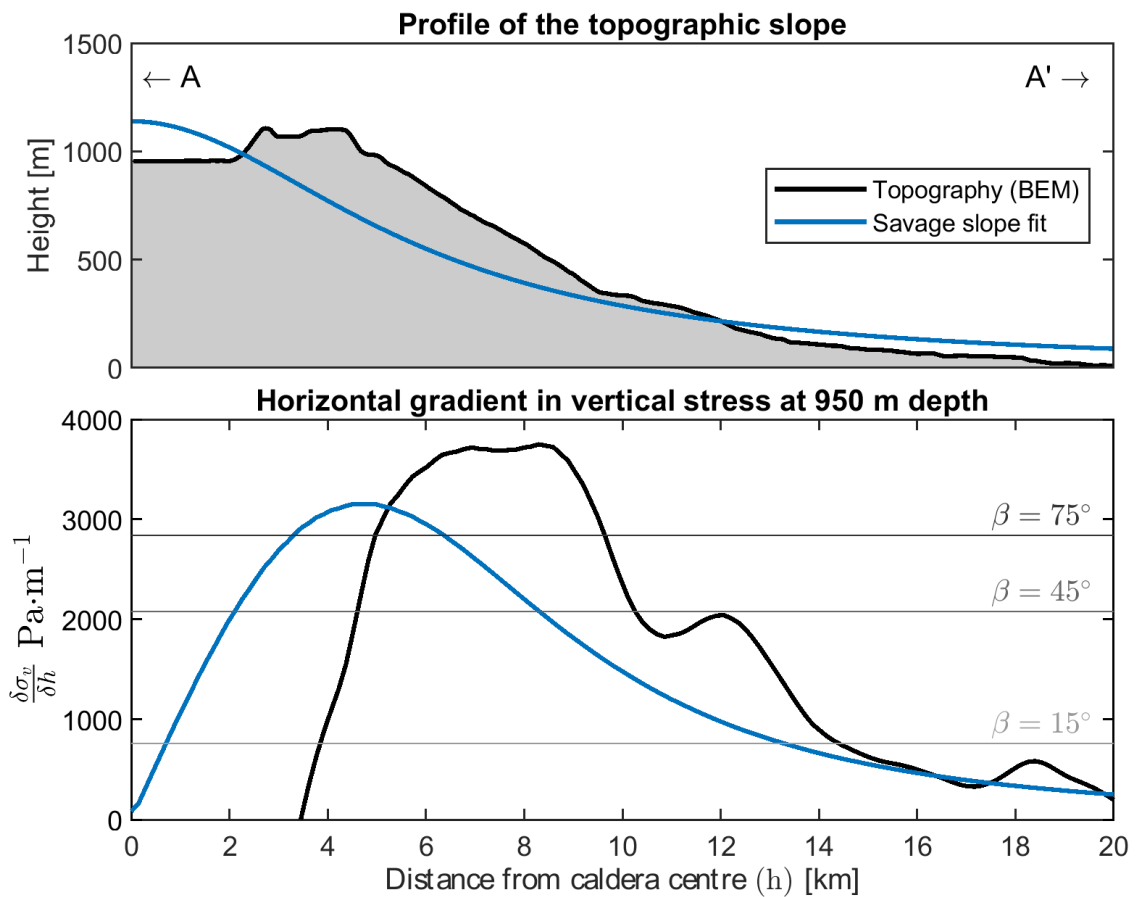
Extended Data Fig. 2. Interferograms of Sierra Negra spanning the sill propagation phase of the 2018 eruption. SAR data are from the Sentinel-1 satellite. Same colourbar as Fig. 1, with each colour cycle as 2.8 cm of LOS ground displacement. Black arrows show the satellite orbit direction, a) \sim S-N b) \sim N-S, look direction a) \sim W-E b) \sim E-W, and the incidence angle in degrees. a) Ascending pass, Track 61 TOPS mode. b) Descending pass, Track 106, TOPS mode. Symbols as in Fig. 1 in the main text.



Extended Data Fig. 3. Interferograms of Sierra Negra spanning the whole propagation and early eruption phase of the 2018 eruption. SAR data are from the ALOS-2 satellite. Colourbar as Fig. 1, with each colour cycle as 11.45 cm LOS ground displacement. Black arrows show the satellite orbit direction, a) \sim S-N b) \sim N-S, look direction a) \sim W-E b) \sim E-W, and the incidence angle in degrees. a) Ascending pass, Track 41, Fine Stripmap mode (SM3; pixel resolution 9.1x5.3 m). b) Descending pass, Track 147, Ultra-fine Stripmap mode (SM1; pixel resolution 3.0x3.0 m). Symbols as in Fig. 1 in the main text.



Extended Data Fig. 4. Magnitude of stress gradients, topographic vs buoyancy. Top panel shows in black the topographic profile of the volcano (profile A-A' in Fig. 2) and in blue an approximation of this profile used to calculate the analytical solution¹³. Bottom panel shows the required crack dip β such that the two competing gradients match, according to $(\rho_r - \rho_f)g \sin(\beta) = \delta\sigma_v/\delta h$. Plane strain boundary element method result due to the topography is shown in black, the result of the analytical solution¹³ due to the approximate slope shown is shown in blue.

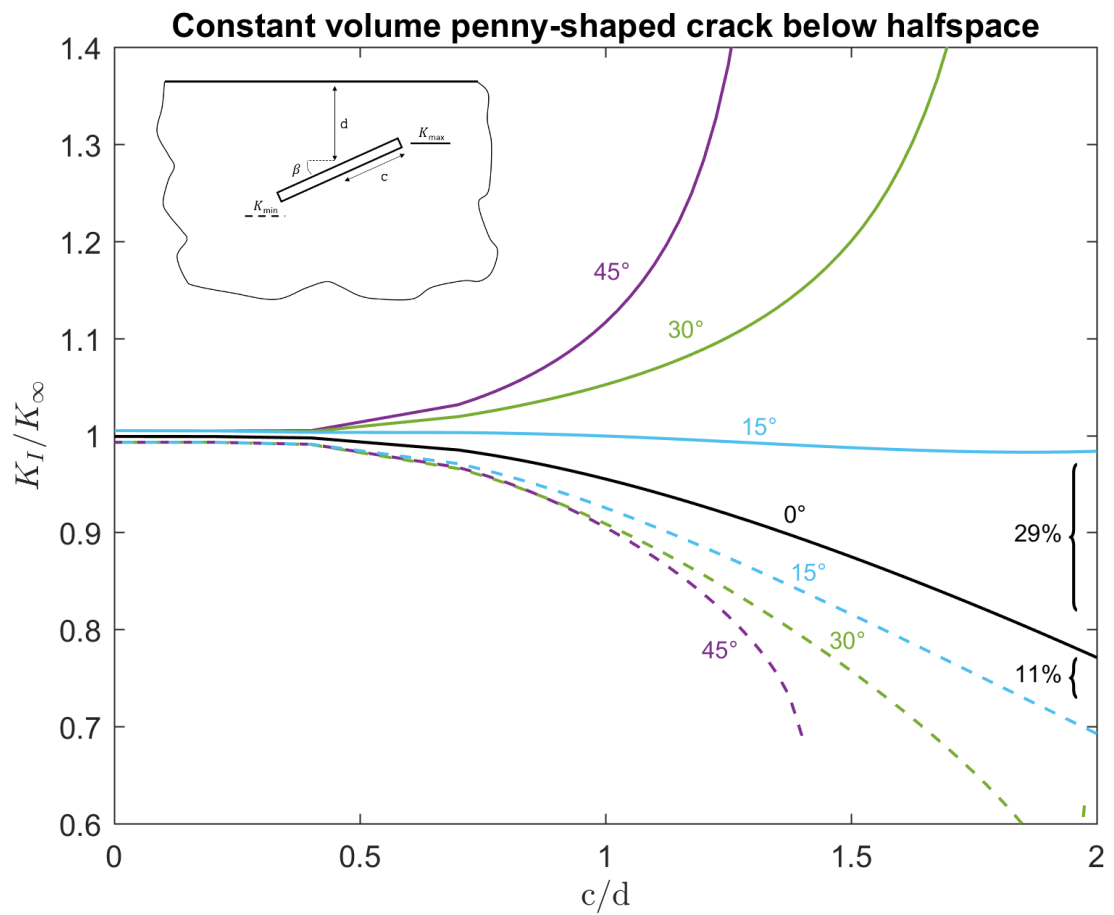


Extended Data Fig. 5. Half-space effects on K_I at the upper and lower tips of a dipping penny-

shaped crack. Maximum and minimum K_I values (solid and dashed) for constant volume cracks, depth d

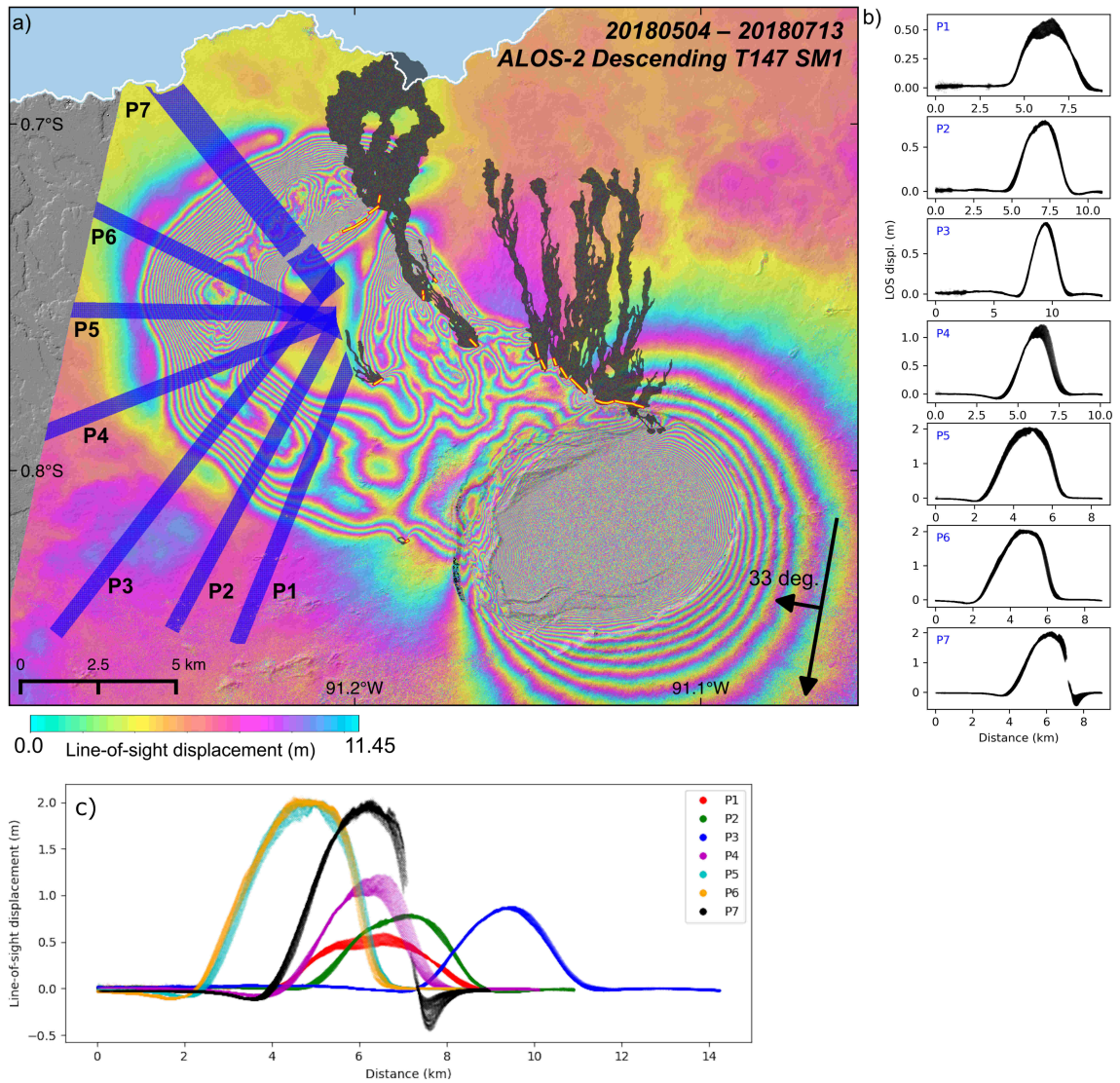
below a half-space, with radius c . Values relative to K_∞ , equation (1)). Note the offset from 1 when $c/d=0$,

indicates the size of the numerical error.



Extended Data Fig. 6. Profiles used to estimate intrusion geometry. a) InSAR as in Extended Data

Fig. 3 with the location of the profiles (P1 - P7) marked by blue shading. Gray polygons show the extent of the lava flows emplaced during the time period spanned by the interferogram. Yellow lines mark the location and extent of all eruptive fissures. b) Each plot shows the line-of-sight ground displacement for each data point included in profiles 1-7. Vertical scale is not constant. c) All profiles shown on one plot, (~ W-E).



Extended Data Fig. 7. Summary of changes in K due to different effects on the sill at Sierra Negra.

Cross sections of cracks showing changes in stress intensity, K_I , at the crack tip due to different processes.

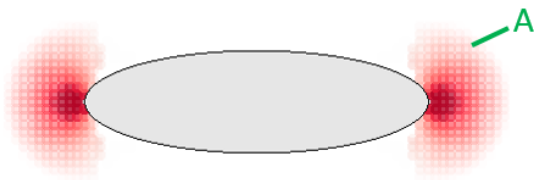
Crack opening exaggerated by 300, red patches show the 2nd invariant of stress computed from K at the tip.

a) crack in a full space, b) crack under topographic stress gradient, topography exaggerated, c) crack with 15°

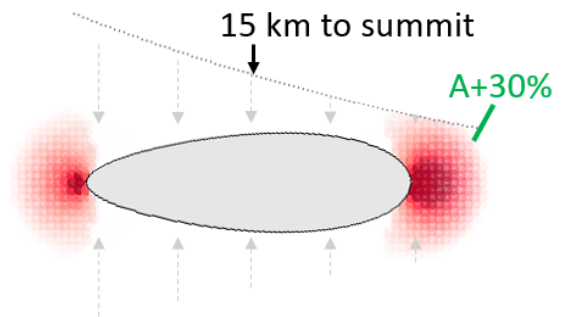
dip, buoyancy as defined in text, d) interacting cracks with separation defined in text, e) flat crack close to the

free surface, f) crack close to free surface with dip, only internal pressure.

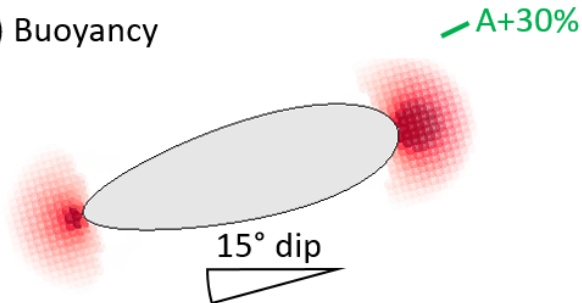
a) Isolated crack full-space



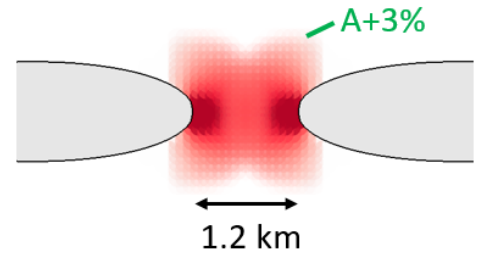
b) Topographic weight



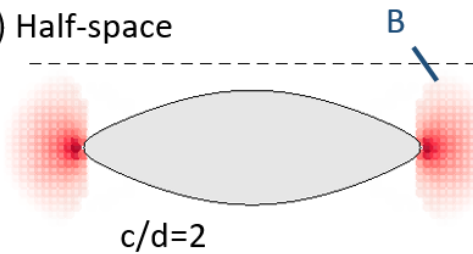
c) Buoyancy



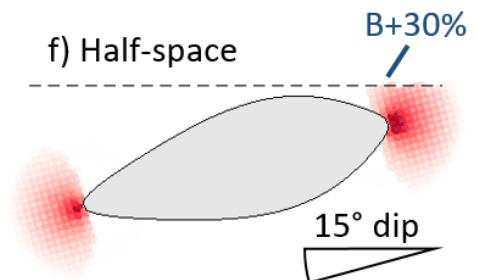
d) Interaction



e) Half-space

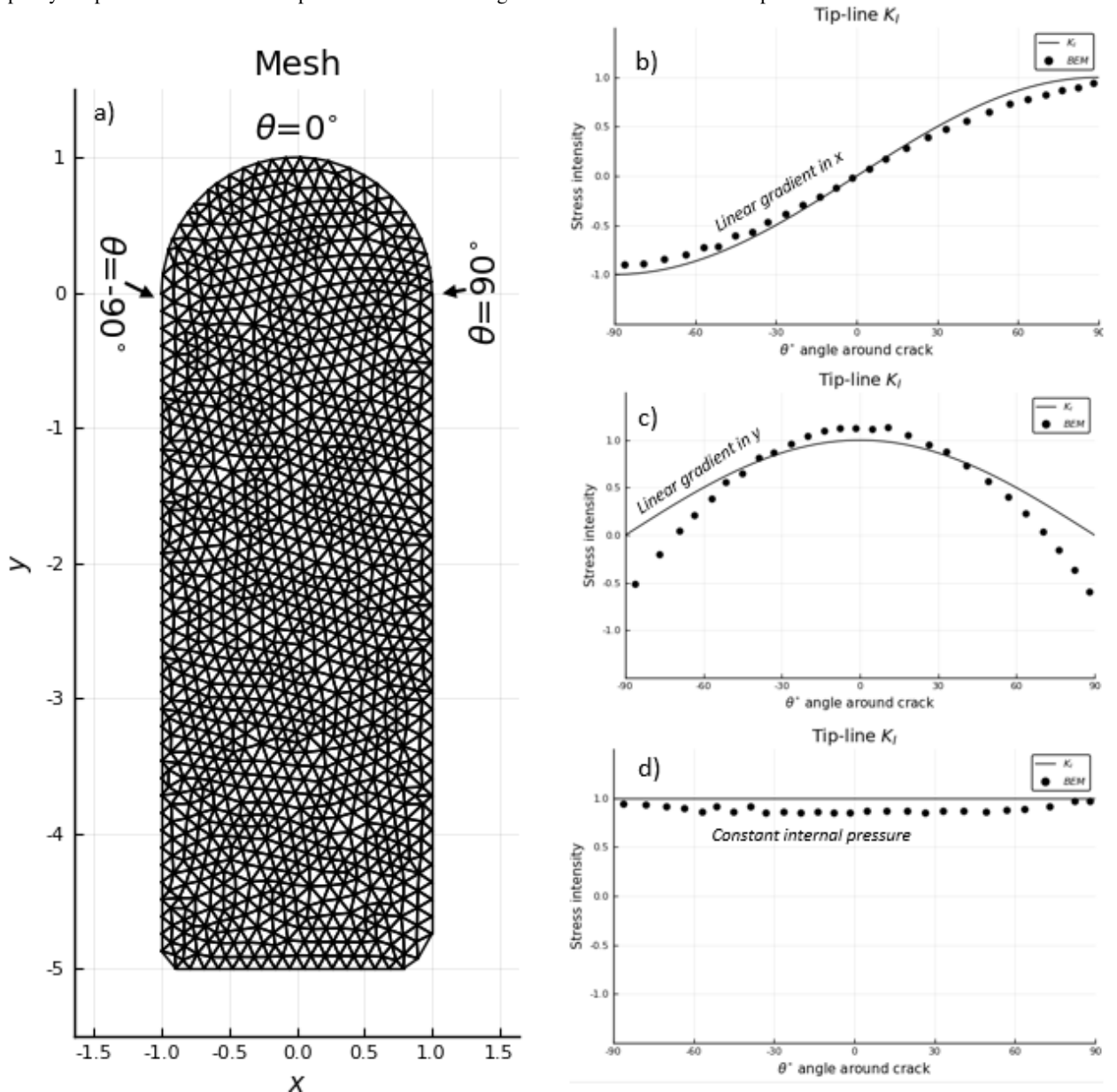


f) Half-space

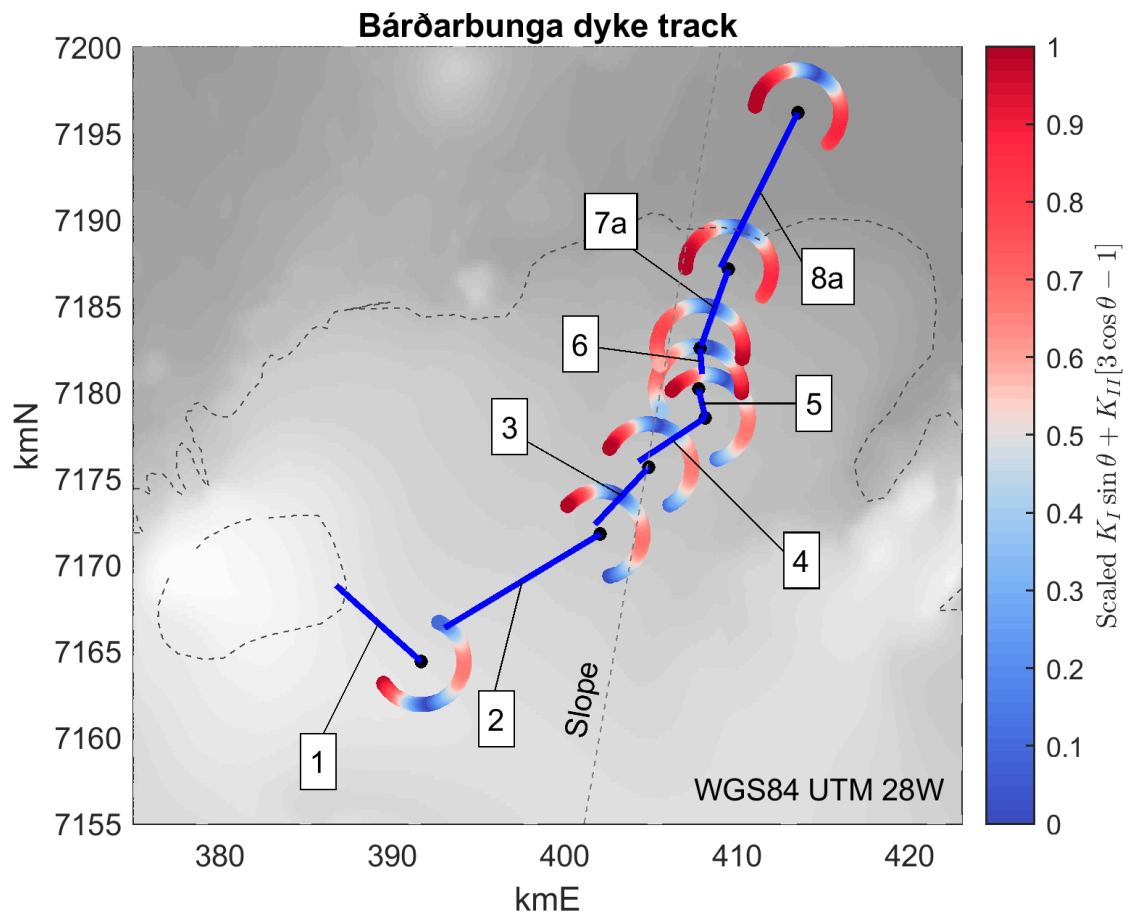


Extended Data Fig. 8. Comparison of K_I around a penny-shaped and elongated penny-shaped crack.

a) The mesh used for this analysis. θ is defined in degrees away from the tip ($y = 1$). Comparison of K_I from equation (2) to that for an elongated penny-shaped crack as in a), assuming b) a stress gradient along the x -axis; c) a stress gradient along the y -axis. d) Comparison of K_I from equation (1) to that for an elongated penny-shaped crack with uniform pressure. Note some slight numerical inaccuracies are present.



Extended Data Fig. 9. Forecasting propagation directions along the Bárðarbunga dyke track. Numbered labels indicate the position of the penny at test locations³. Preferred directions of propagation, according to equation (SI.2), where the maximum circumferential (hoop) stress is shown in blue.



342

343

Supplementary Information

344

Approximating the sill geometry as a penny

345

346

347

348

349

350

351

352

353

354

355

Here we estimate the error associated with approximating a 3D propagating crack as penny-shaped. We compare analytical formulas that describe K around the tip-line of penny-shaped cracks under uniform pressure and linear stress gradients, equation (1 & 2) to those of a more realistic 3D shape (Extended Data Fig. 8a). We apply boundary conditions so that the opening of lengthened-tail crack matches that of the penny-shaped crack, at the location where the penny's opening is maximal. For penny-shaped cracks with constant internal pressure this is the crack centre. For a penny-shaped crack under a linear stress gradient the maximal opening is located along the direction of the stress gradient at $\sin(\pi/4)c$. We find the analytical formulas capture the scale and shape of the problem with some deviations (Extended Data Fig. 8b, c and d). Note the accuracy of the numerical boundary element method to approximate K can have errors of up to 10% and the mesh used in Extended Data Fig. 8 has ~ 2000 triangles^{9,10}.

356

Reproducing Bárðarbunga's track

357

358

359

Here we test our analytical approach of approximating the crack as a series of isolated pennies on the case of the Bárðarbunga 2018 dyke track. The aim is to test how well the assumptions of our method perform in comparison to methods that take into account the entire dyke surface³.

360

361

362

363

364

365

366

We use a series of vertical pennies with $c=2000$ m, $d=4000$ m, $V=3\pi c^2$ m³ (i.e. opening of 3 m if constant), $\nu=0.25$, $\mu=2\cdot 10^9$ Pa. All stresses are evaluated at the crack centre. We define the tectonic stress as that due to a vertical semi-infinite buried dislocation³ of 4 m opening with an upper tip depth of 10 km, centred at Askja volcano and striking at 12°. As before, we use an analytical solution describing stresses beneath topographic slopes using a state of perfect confinement¹³, applied along the straight dashed line shown in Extended Data Fig. 9. K_I around the tip-line is defined by the internal volume through equation (1), and by the gradient in normal trac-

367 tion taken from the slope stress solution, equation (2). Shear stresses due to the tectonic and grav-
 368 itational stresses are resolved as shear traction (t_s) on the plane of the dyke at its centre and K_{II}
 369 is computed with:

$$K_{II} = \frac{4t_s\sqrt{c/\pi}}{2-\nu} \quad (\text{SI.1})$$

370 We compute K at the leading tip of the penny (black dots in Extended Data Fig. 9). Free surface
 371 effects on values of K_I and K_{II} are below 10%, even with c/d ratios of 0.99. Turning of the lead-
 372 ing tip is then computed using:

$$K_I \sin \theta + K_{II}(3 \cos \theta - 1) \quad (\text{SI.2})$$

373 where the minimum value corresponds to the direction of the greatest circumferential stress ($\theta_0=0$)
 374 close to the tip, and as such the potential propagation direction¹⁸. We find our analytical approach
 375 predicts the dyke's pathway in a computationally efficient way (Extended Data Fig. 9).

376 **Supplementary material references**

- 377 3. Sigmundsson, F. *et al.* Segmented lateral dyke growth in a rifting event at Bárðarbunga
 378 volcanic system, Iceland. *Nature* **517**, 191–195 (2015).
- 379 9. Davis, T., Healy, D. & Rivalta, E. Slip on wavy frictional faults: Is the 3rd dimension a
 380 sticking point? *Journal of Structural Geology* **119**, 33–49 (2019).
- 381 10. Davis, T., Rivalta, E. & Dahm, T. Critical fluid injection volumes for uncontrolled frac-
 382 ture ascent. *Geophysical Research Letters*, e2020GL087774 (2020).
- 383 13. Savage, W. Z., Powers, P. S. & Swolfs, H. S. *In situ geomechanics of crystalline and sed-*
 384 *imentary rocks; Part V, RVT, a Fortran program for an exact elastic solution for tecton-*
 385 *ics and gravity stresses in isolated symmetric ridges and valleys* tech. rep. (US Geolog-
 386 ical Survey, Denver, Colorado, 1984).

- 387 18. Pollard, D., Pollard, D. D., Fletcher, R. C. & Fletcher, R. C. *Fundamentals of structural*
388 *geology* (Cambridge University Press, 2005).